

Research Article

Research and Application of Heavy-Equipment Parachute Rope Tension Sensor

Min Yao , Yanhua Jin, Min Zhao, and Shaohua Xu

College of Automation Engineering, Nanjing University of Aeronautics and Astronautics, Nanjing, China

Correspondence should be addressed to Min Yao; ym_nuaa@163.com

Received 9 May 2018; Revised 8 September 2018; Accepted 22 October 2018; Published 30 December 2018

Academic Editor: Abdellah Touhafi

Copyright © 2018 Min Yao et al. This is an open access article distributed under the Creative Commons Attribution License, which permits unrestricted use, distribution, and reproduction in any medium, provided the original work is properly cited.

Heavy-equipment airdrops are mainly used to deliver relief supplies and heavy weapons. Given the heavy weight of the goods, the tension of the extraction and brake ropes of the parachute significantly affects the safety of the aircraft. On the basis of the measurement and installation characteristics of the parachute rope, this study designed the structure of a nondestructive pressure-type parachute rope tension sensor and set the location of the strain gauge patch using the ANSYS simulation software to obtain a high sensor sensitivity. The temperature error of the tension sensor is compensated, and the precision is improved using the LSSVM-PSO (Least Squares Support Vector Machine-Particle Swarm Optimization) algorithm. The developed tension sensor is applied to the extraction parachute test system to measure the traction of 2 and 8 m² parachutes. Test results show that the maximum weight of the platform these two parachutes can draw and the effect of parachute opening can be calculated.

1. Introduction

In recent years, large transport aircrafts have rapidly developed, improving the conditions for heavy-equipment airdrops and increasing the demands on the airdrop system [1–3]. The heavy-equipment airdrop system is mainly used by large- and medium-sized transport aircrafts in delivering heavy weapons, equipment, emergency supplies, and other goods to the designated area to support land and naval operations or disaster relief work [4, 5].

In the process of heavy-equipment airdrop, pulling the platform out of the cabin requires a large pulling force of the extraction parachute. Meanwhile, the large tension generated by the parachute affects the safety of the transporting aircraft. Therefore, the tension of the parachute rope during the operation of the parachute is closely related to the platform and the smooth flight of the transport aircraft.

However, such large tension sensors for parachute ropes of heavy-equipment airdrop systems are rarely reported. Zhao et al. from Nanjing University of Aeronautics and Astronautics designed the surface acoustic wave tension sensor for parafoils in 2017 [6]. This sensor has good linearity

and repeatability. However, this sensor system needs a reader to send and receive wave signals, which makes the measurement extremely sensitive to interference. Lu et al. from Xidian University designed a compensated SAW sensor to measure the yarn tension [7]. The measurement range is no more than 1 N, and its structure is not suitable for installing in parachute ropes.

The tension sensors for parachute ropes of heavy-equipment airdrop systems may have the same structure as the tension sensors for vehicle safety belts, such as the EL20-S458 sensor produced by U.S. MEAS and LBT-A-20KNSA1 produced by KYOWA. However, this structure has distinct edges and corners. The friction of the sensors may cause damage to the parachute ropes or even burn the ropes. This structure is difficult to install and the rope needs to be cut, all of which are unsuitable for parachutes. Furthermore, the detection range of such sensors for the automotive belt is unsuitable for the heavy-equipment airdrop test.

This study designed a kind of nondestructive tension sensor for the measurement of the tension of extraction and brake parachute ropes. The proposed tension sensor is characterized by wide range, high precision, and easy installation.

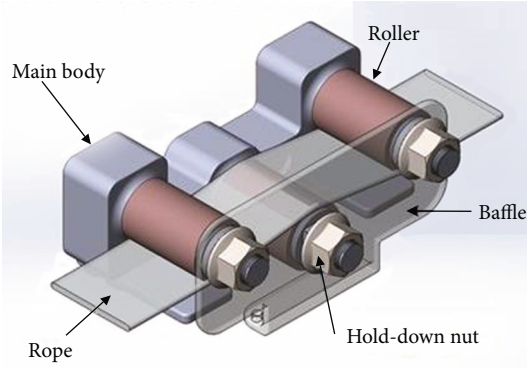


FIGURE 1: Structure of the tension sensor.

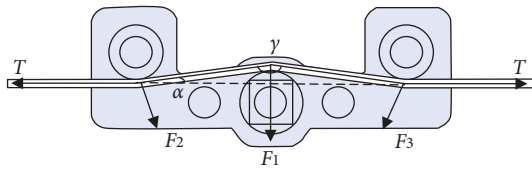


FIGURE 2: Force analysis of the tension sensor.

2. Force Analysis and Structure Design

It is necessary to test the parachutes rigorously before they are put into use. The tests include parachute control performance evaluation, smooth sliding performance evaluation, and stability test. In order to realize these tests, the measurement of the stress of each rope during landing is very important. It reflects the force of the ropes and the degree of stress equalization. It is also an important indicator of parachute control performance.

The overall structure of the tension sensor is shown in Figure 1. The sensor is designed as a three-axis compression type, which consists of four parts, namely, the main body, roller, baffle, and nut. A cylinder roller is used in this sensor to ensure that it is nondestructive and it can help to reduce weight. The roller can effectively reduce the contact area with the parachute ropes and the friction of the sensors.

As shown in Figure 1, the parachute rope is installed and fixed on the side of the sensor. After the parachute rope is stressed, the sensor is tightened and pressed. Then, the parachute rope transmits the force to the sensor and undergoes elastic deformation. The stress on the sensor body is uneven, and the location of the strain gauge is an important part of the design. Sufficient strain should be provided to ensure the sensitivity of the sensor and meet the measurement range. Therefore, force analysis of the sensor structure is required to determine the locations of the strain gauges.

The mechanical structure model of the sensor structure is shown in Figure 2. Assuming that the ropes are subjected to tensile force T , the forces acting on the two rollers of the sensor due to the straightening of the ropes are shown in Figure 2. F_1 , F_2 , and F_3 are the pressures applied to the sensor structure by the belt tension, and α is the initial belt tension angle.

According to the sensor force diagram shown in Figure 2, the following equations are derived:

$$|F_1| = 2|T| \sin \alpha, \quad (1)$$

$$|F_2| = |F_3| = 2|T| \sin \left(\frac{\alpha}{2} \right). \quad (2)$$

According to Equations (1) and (2), the sensor sensitivity and range are related to the angle α . The smaller the angle α is, the lower the sensitivity of the sensor is and the larger the measurement range is. In finding the sensor to meet the range of the premise, increasing the angle as much as possible under the condition of meeting the range of the sensor is necessary.

The material of the sensor is 42CrMo. Figure 3(a) shows the ANSYS grid meshing, and Figure 3(b) shows the strain analysis. The stress distribution diagram shows the maximum stress areas in red. These areas are the combination of the middle guide cylinder and the force beam, which is consistent with the actual structure. The structure of the beam arm suffers from a high degree of stress, such that the location of the beam arm is selected as the installation position of the strain gauge. The glue patch location is shown in Figure 4.

Strain gauges are widely used in strain measurement [8, 9]. The strain gauge used in this sensor is BE650-4BB (11), the structure of which is shown in Figure 5. The two gantries perpendicular to each other in the "T" gauge are used for the axial and transverse direction train measurements, also known as Poisson strain.

As shown in Figure 4, in position 1, a strain gauge is attached to each force arm. The tension sensor detects four resistances on each force arm, i.e., axial resistance changes ΔR_{x1} and $\Delta R'_{x1}$ and transverse resistance changes ΔR_{y1} and $\Delta R'_{y1}$. Position 1 is opposite to position 2 in terms of strain direction. ΔR_{x1} and ΔR_{y1} are the resistance changes of the left force arm, and $\Delta R'_{x1}$ and $\Delta R'_{y1}$ are the resistance changes of the right force arm, as shown in Figure 4. Overall, these eight resistances can produce two four-arm bridges, as shown in Figure 6.

According to the four-arm bridge principle, the output is derived as follows:

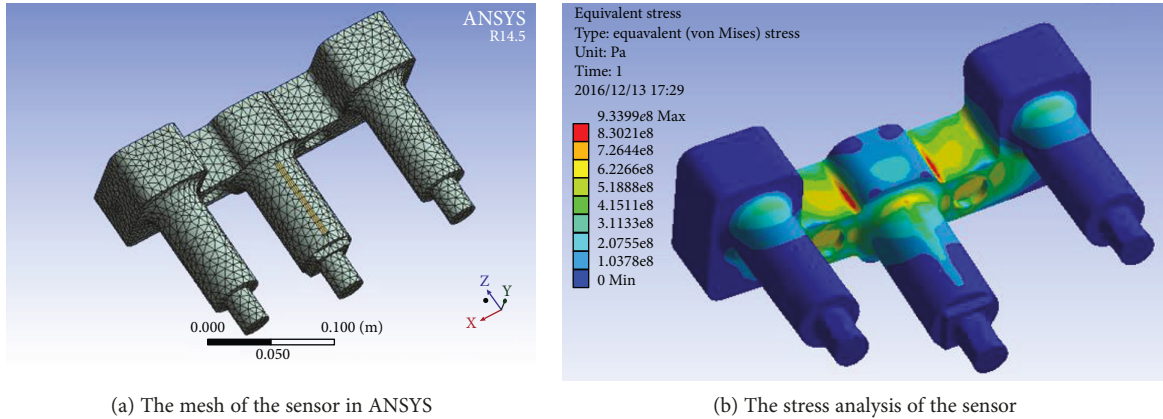
$$U_{\text{out}} = \frac{1}{8} UK \left[\varepsilon_{x_1} + \varepsilon_{y_1} - \left(\varepsilon_{x_2} + \varepsilon_{y_2} \right) \right]. \quad (3)$$

In Equation (3), U_{out} is the output voltage of the bridge, K is the sensitivity coefficient of the strain gauge, and ε is the strain.

From the sensor force shown in Figure 2 and the analysis expressed in Equations (1) and (2), when the sensor receives a certain amount of tension T , ε can be related to α in this sensor structure.

3. Temperature Error Compensation

The sensor is designed for testing the heavy-equipment airdrop extraction parachute and will measure the pulling



(a) The mesh of the sensor in ANSYS

(b) The stress analysis of the sensor

FIGURE 3: Stress analysis of the sensor by the ANSYS software.

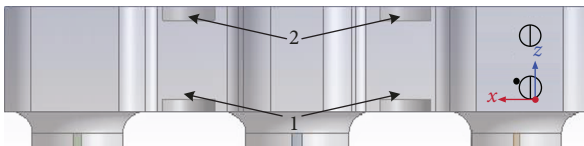


FIGURE 4: Strain gauge patch diagram.

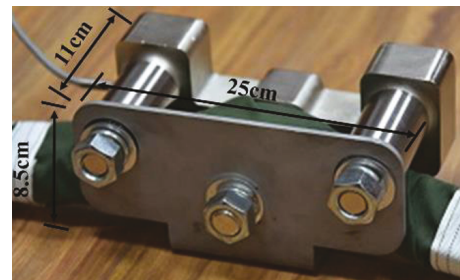


FIGURE 7: The sensor system.

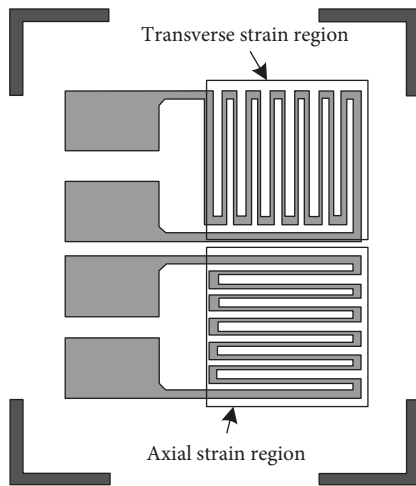


FIGURE 5: Diagram of the strain gauge.

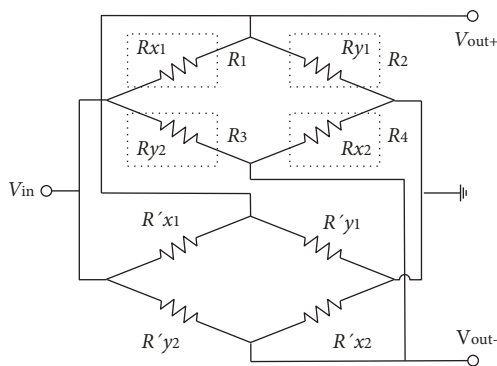


FIGURE 6: Measurement circuit.

force of the platform on the rail out of the plane. The range of traction is 0–100 kN. The sensor system is shown in Figure 7.

Temperature error is one of the main errors of the strain sensor [10–12]. The airdrop height will vary from hundreds of meters to thousands of meters, so that the temperature will change in a wide range. Therefore, the temperature error of the parachute tension sensor cannot be ignored.

The measurement of the strain gauge may be affected by many factors, such as temperature, vibration, and transverse effect. These factors cause a nonlinear error and the temperature is one of the key factors. A traditional temperature compensator is usually used to decrease the temperature error. However, other nonlinear errors caused by other factors are not fully considered [13]. A BP neural network is also used in nonlinear compensation [14]. This method has higher precision, but it does not fully consider the influence of temperature. Nagi et al. used support vector machines and a genetic algorithm to compensate for the nonlinear error [15], but the process of coding, crossover, selection, and variation increases the complexity of the algorithm. In this paper, LSSVM and particle swarm optimization are combined to compensate for the nonlinear error of the tension sensor, especially the temperature error. LSSVM-PSO algorithm maps the input vector to a high-dimensional feature space via nonlinear mapping and constructs the optimized decision function [16–18]. The PSO algorithm featured with memory functions is used to search for optimal value. In this way, it can efficiently reduce calculation complexity and solve nonlinear problems of small samples.

The resistance variation of the strain gauge is the combination of the resistance changes ΔR_E , which is caused by load deformation, and ΔR_T , which is caused by temperature change, and is expressed as follows:

$$\Delta R = \Delta R_E + \Delta R_T. \quad (4)$$

The strain caused by the temperature is influenced by the temperature coefficient of resistance of the strain gauge. When the temperature changes ΔT , the relative variation of the strain gauge can be expressed as follows:

$$\frac{\Delta R_T}{R} = \alpha_R \Delta T. \quad (5)$$

In Equation (5), α_R is the temperature coefficient of resistance of the strain material. In Figure 6, according to the bridge principle, ΔR_{x1} and $\Delta R'_{x1}$ are the axial resistance variations and ΔR_{y1} and $\Delta R'_{y1}$ are the lateral variations. Assuming that the strain errors of each strain gauge are the same, the lateral resistance variation error is δ and the longitudinal variation error is $-\delta$. According to Equations (3), (4), and (5), the result is derived as follows:

$$U_{\text{out}} = \frac{1}{2} U \delta \left[(1 + 2\mu) \frac{dL}{L} + \alpha_R \Delta T \right]. \quad (6)$$

In building an LSSVM model with good adaptability, the test takes the tension sensor data from different environments such as training samples, with sensor output U and environmental temperature T as inputs. The sample set Q is built as follows:

$$Q = \{(x_1, y_1), (x_2, y_2), \dots, (x_i, y_i), i = 1, \dots, n\}. \quad (7)$$

In Equation (7), x_i is the i th input, i.e., $x_i = [T_i, U_i]$, and y_i is the algorithm output. The LSSVM model of data approximation can be expressed as follows:

$$\begin{cases} \min & J(\omega, \xi) = \frac{1}{2} \omega^T \omega + \frac{1}{2} \gamma \sum_{i=1}^n \xi_i^2 \\ \text{s.t.} & \beta_i = \omega^T \varphi(x_i) + b + \xi_i, \\ & i = 1, \dots, n. \end{cases} \quad (8)$$

In Equation (8), J is the pending optimized function, ω is the weight vector, $\varphi(x)$ is the nonlinear mapping function, γ is the regularization parameter, and b is the deviation value. The following Lagrangian function is introduced to derive the constrained optimal solution:

$$L(\omega, b, \xi, a) = \frac{1}{2} \omega^T \omega + \frac{1}{2} \gamma \sum_{i=1}^n \xi_i^2 - \sum_{i=1}^n a_i [w^T \varphi(x_i) + b + \xi_i - \beta_i]. \quad (9)$$

The parameter a_i is introduced in Equation (9) as the Lagrangian multiplier. The partial derivatives of ω , b , ξ ,

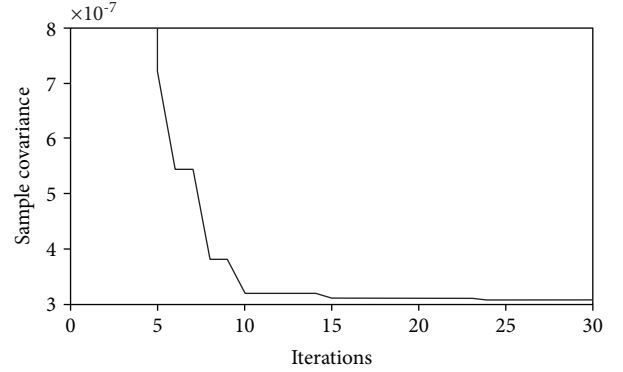


FIGURE 8: PSO optimal curve.

and a should be equal to 0 to obtain the extreme value using Equation (9). The linear equation set is generated as follows:

$$\begin{bmatrix} 0 & 1 & \cdots & 1 \\ 1 & K(x_1, x_1) + \gamma^{-1} & \cdots & K(x_n, x_1) \\ \vdots & \vdots & \ddots & \vdots \\ 1 & K(x_1, x_n) & \cdots & K(x_n, x_n) + \gamma^{-1} \end{bmatrix} \begin{bmatrix} b \\ a_1 \\ \vdots \\ a_n \end{bmatrix} = \begin{bmatrix} 0 \\ \beta_1 \\ \vdots \\ \beta_n \end{bmatrix}. \quad (10)$$

$K(x, x_i)$ is the kernel function of the LSSVM algorithm. In this study, the radial basis kernel function of strong generalization is selected by mapping the original feature into the indefinite dimensions. The expression is as follows:

$$K(x, x_i) = \exp \left(-\frac{\|x - x_i\|^2}{\sigma^2} \right). \quad (11)$$

The values of b and the Lagrangian multiplier a_i can be derived from the Lagrangian function. The tension sensor compensation model, i.e., the nonlinear approximation of the LSSVM model, is expressed as follows:

$$f(x_i) = \sum_{i=1}^n a_i K(x, x_i) + b. \quad (12)$$

In the LSSVM model, parameters $[\sigma, \gamma]$ require optimization. Sample covariance e_{RMSE} is the objective function in the PSO algorithm. When the sample covariance reaches the set precision, the corresponding parameters

TABLE 1: Temperature error of the sensor without compensation.

Tension (kN)	$V_{out} (V)$							Err _{temp} (%FS)
	-20°C	-10°C	0°C	+10°C	+20°C	+30°C	+40°C	
0	0.012	0.015	0.017	0.017	0.019	0.025	0.044	0.50%
20	0.969	0.972	0.991	1.003	1.011	1.020	1.034	0.84%
40	1.930	1.942	1.961	1.985	2.006	2.198	2.041	1.52%
60	2.892	2.920	2.953	2.962	2.975	3.021	3.033	1.66%
80	3.859	3.870	3.894	3.908	3.925	3.940	3.956	1.32%
100	4.817	4.833	4.845	4.857	4.862	4.882	4.896	0.90%

TABLE 2: Temperature error of the sensor with compensation.

Tension (kN)	$V_{out} (V)$							Err _{temp} (%FS)
	-20°C	-10°C	0°C	+10°C	+20°C	+30°C	+40°C	
0	0.041	0.032	0.028	0.022	0.019	0.021	0.043	0.48%
20	0.998	1.005	1.007	1.010	1.011	1.014	1.019	0.26%
40	1.964	1.973	2.002	1.997	2.006	2.004	2.000	0.84%
60	2.932	2.961	2.958	2.971	2.975	2.982	2.973	0.86%
80	3.905	3.913	3.912	3.924	3.925	3.928	3.930	0.40%
100	4.875	4.863	4.857	4.867	4.862	4.870	4.881	0.38%

$[\sigma, \gamma]$ can be regarded as the global optimal solution. The sample covariance e_{RMSE} is expressed as follows:

$$\begin{aligned}
 e_{RMSE} &= \left[\frac{1}{n} \sum_{i=1}^n (f(x_i) - y_i)^2 \right]^{1/2} \\
 &= \left[\frac{1}{n} \sum_{i=1}^n \left(\sum_{i=1}^n a_i K(x, x_i) + b - y_i \right)^2 \right]^{1/2}. \quad (13)
 \end{aligned}$$

We assume that the size of the particle in the D -dimensional search space is M , the position of the i th particle is x_i , and the flight speed is v_i . In the n th iteration, the historical optimal position of the particle is P_{best} and the optimal position of the global particles is g_{best} . The iterative formula is expressed as follows:

$$\begin{cases} V(t+1) = \omega V(t) + c_1 r_1 [P(t) - X(t)] + c_2 r_2 [P(t) - X(t)], \\ X(t+1) = X(t) + \lambda V(t+1). \end{cases} \quad (14)$$

In Equation (12), t is the current evolution algebra, c_1 and c_2 are the nonnegative factors, ω is the inertia weight, λ is the speed factor, and r_1 and r_2 are the random numbers within $[0,1]$. We set $D=2$, $M=25$, $[c_1, c_2] = [2, 0.8]$, and $\lambda=1$. 25 stacks of measured data of the tension sensor tested in different temperatures were brought into the PSO algorithms as samples to search for the optimal results. The optimization process is shown in Figure 8. When the PSO algorithm reaches 24 iterations, the sample covariance e_{RMSE} is

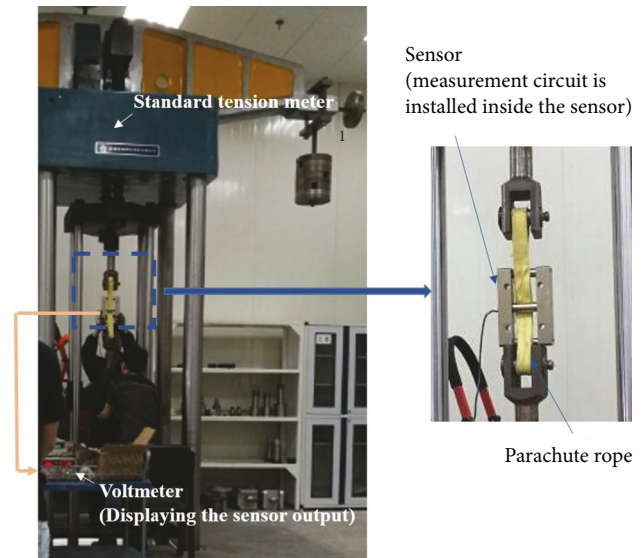


FIGURE 9: The picture of the test.

3.084×10^{-7} and the pending optimal parameters are $[\sigma, \gamma] = [2.181, 1.395]$.

The tension sensor with the full range of 100 kN was kept in a high- and low-temperature environment for 30 minutes before the test. As the standard tension meter has a large volume, it is difficult to put the whole testing system into a constant temperature environment. Therefore, the tension sensor is processed separately to get different working temperatures and we get its exact working temperature with a temperature sensor stuck to the tension sensor during the test.

TABLE 3: The parameters of the standard tension meter and the voltmeter used in the test.

Equipment name	Range	Precision
Standard tension meter	1–100 kN	0.01%
Voltmeter	DC: (0–1000 V), AC: (0–750 V)	DC: 0.01%, AC: 0.1%

TABLE 4: The results of the test in room temperature (temperature: 20°C, humidity is 62% RH).

Standard force value (kN)	Uptravel output (V)				Repeatability (%FS)	Theoretical value (V)	Nonlinearity (%FS)	Downtravel output (V)			Precision (%FS)
	1	2	3	Average				1	2	3	
0	0.039	0.008	0.011	0.019	0.64	0.019	0.00	0.007	0.012	0.017	0.41
20	1.037	0.991	1.005	1.011	0.95	0.988	0.47	1.056	1.020	1.037	1.40
40	2.040	1.978	2.001	2.006	1.28	1.956	1.03	2.085	2.030	2.068	2.65
60	3.006	2.942	2.977	2.975	1.32	2.925	1.03	3.072	3.130	3.065	2.88
80	3.942	3.893	3.939	3.925	1.01	3.893	0.66	3.975	4.006	4.036	2.94
100	4.860	4.831	4.896	4.862	1.34	4.862	0.00				0.70

Temperature error calculation is as follows:

$$\text{Err}_{\text{temp}} = \frac{V_{\text{out}} - V_{20^\circ\text{C}}}{V_{\text{FS}}}, \quad (15)$$

where V_{out} is the output of the sensor system in any temperature, $V_{20^\circ\text{C}}$ is the output of the sensor in room temperature (20°C), and V_{FS} is the full scale of the output.

Table 1 shows the test data in the range of 0–100 kN at room temperature (+20°C), high temperature (+40°C), and low temperature (−20°C) without compensation.

Three rounds of the tests were carried out. All the data were used to form the training data (x_i, y_i) , as formula (7). $x_i = [T_i, U_i]$ and y_i is the expected output. For example, the data in Table 1 form the training data as follows: $([-20, 0.012], 0.019)$, $([-20, 0.969], 1.011)$, $([-20, 1.930], 2.006)$, $([-20, 2.892], 2.975)$, $([-20, 3.859], 3.925)$, $([-20, 4.817], 4.862)$, $([-10, 0.015], 0.019)$, $([-10, 0.972], 1.011)$, $([-10, 1.942], 2.006)$, $([-10, 2.920], 2.975)$, $([-10, 3.870], 3.925)$, $([-10, 4.833], 4.862)$, $([0, 0.017], 0.019)$, $([0, 0.991], 1.011)$, $([0, 1.961], 2.006)$, $([0, 2.953], 2.975)$, $([0, 3.894], 3.925)$, $([0, 4.845], 4.862)$, $([10, 0.017], 0.019)$, $([10, 1.003], 1.011)$, $([10, 1.985], 2.006)$, $([10, 2.962], 2.975)$, $([10, 3.908], 3.925)$, $([10, 4.857], 4.862)$, $([20, 0.019], 0.019)$, $([20, 1.011], 1.011)$, $([20, 2.006], 2.006)$, $([20, 2.975], 2.975)$, $([20, 3.925], 3.925)$, $([20, 4.862], 4.862)$, $([30, 0.025], 0.019)$, $([30, 1.020], 1.011)$, $([30, 2.198], 2.006)$, $([30, 3.021], 2.975)$, $([30, 3.940], 3.925)$, $([30, 4.882], 4.862)$, $([40, 0.044], 0.019)$, $([40, 1.034], 1.011)$, $([40, 2.041], 2.006)$, $([40, 3.033], 2.975)$, $([40, 3.956], 3.925)$, and $([40, 4.896], 4.862)$.

After training with the LSSVM-PSO algorithm, another round of test was carried out. The output after temperature compensation was shown in Table 2. The test results show that the sensor temperature errors decrease from 1.66% to 0.86% after temperature compensation.

Finally, the sensor was tested and calibrated in Wuxi Institute of Metrology and Testing (WXMTTC). The sensor was tested in high temperature (+40°C), room temperature

(+20°C), and low temperature (−20°C) separately. Figure 9 is the testing picture. The parameters of the testing machine are shown in Table 3.

The sensor was tested for three rounds in room temperature. The room temperature is 20°C, and the relative humidity was 62% RH. The results of the testing are shown in Table 4.

As shown in Table 4, the repeatability of the sensor is 1.34% and the nonlinearity is 1.03%. The precision of the sensor is 2.94%.

Then, the sensor was tested in high temperature (+40°C) and low temperature (−20°C) separately. After the sensor was kept in high temperature/low temperature for 30 minutes, the sensor was tested from 0 to 100 kN. The test results for high/low temperature are shown in Table 5.

As shown in Table 5, the precision of this sensor in high temperature and low temperature is 2.46%. Temperature has a very small influence on this sensor.

4. Traction Test for Heavy-Equipment Airdrop Extraction Parachute

The proposed sensor was applied to the extraction parachute traction test of large transport aircrafts. The test measured the pulling force of the parachute when the cargo was dragged out of the aircraft cabin in the heavy-weaponry system. The traction test platform is shown in Figures 10 and 11. The heavy-weaponry system requires a tremendous force to drag the cargo out of the cabin for airdrop, which usually uses an extraction parachute. Different extraction parachutes generate varied pulling forces. Each type of transport aircraft equipped with the corresponding type of extraction parachute according to cargo weight must pass rigorous tests. On one hand, the appropriate traction force ensures that the cargo is dragged out of the cabin successfully. On the other hand, the tremendous pulling force, particularly at the moment of opening the parachute, cannot influence the safety of flight [19, 20].

TABLE 5: The results of the test in high/low temperature (high temperature: +40°C, low temperature: -20°C).

Standard force value (kN)	Output (V) -20°C		Output (V) +40°C		Theoretical value (V)	Precision (%FS)
	Uptravel	Downtravel	Uptravel	Downtravel		
0	0.029	0.020	0.012	0.032	0.019	0.27
20	1.022	1.034	1.043	1.056	0.988	1.40
40	2.023	2.044	2.004	2.034	1.956	1.80
60	3.001	3.023	3.009	3.045	2.925	2.46
80	3.931	3.956	3.907	3.942	3.893	1.29
100	4.848		4.817		4.862	0.96

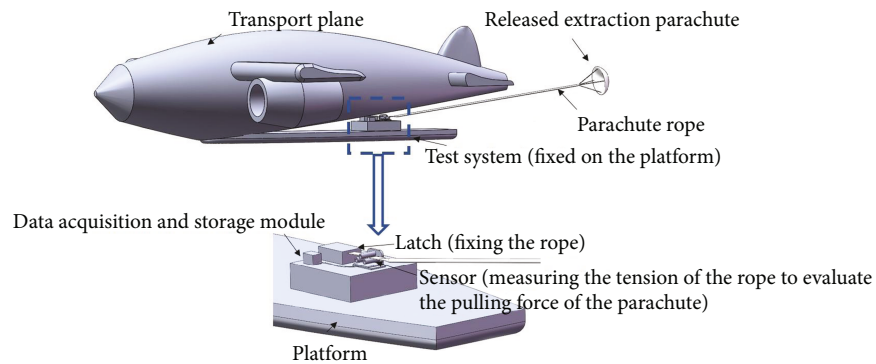


FIGURE 10: Traction test diagram.

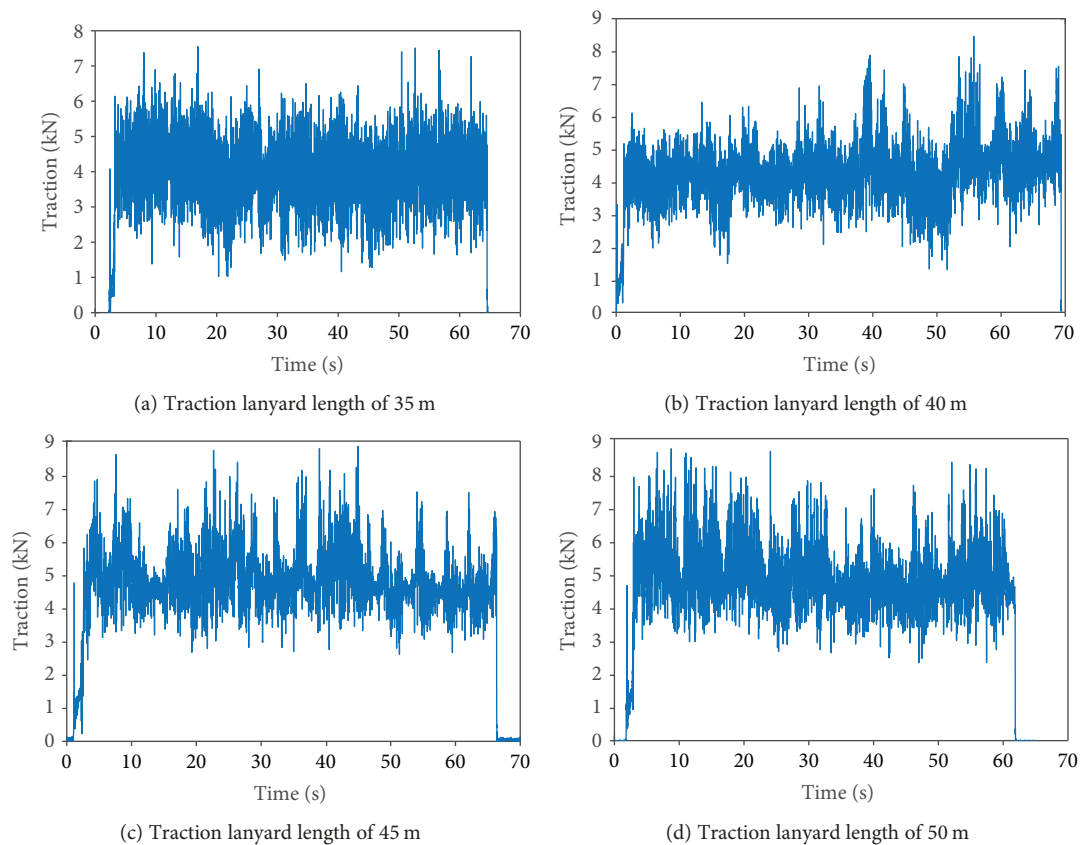
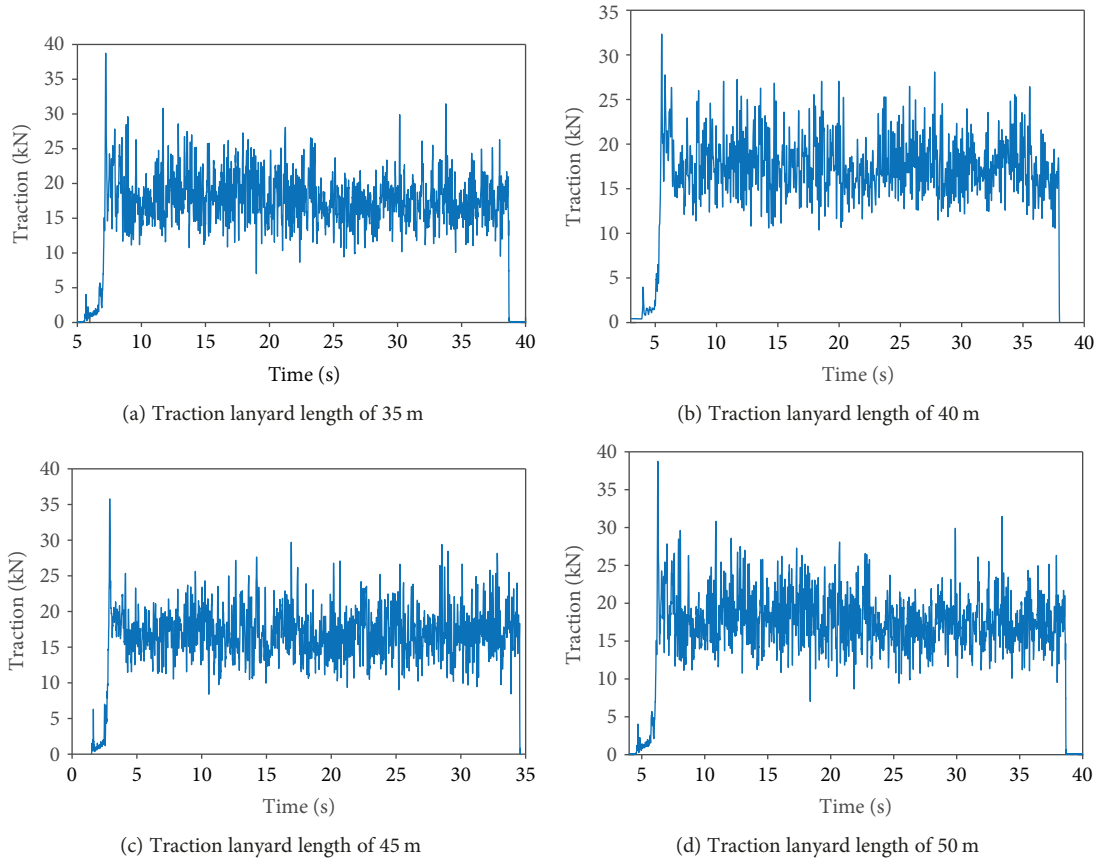


FIGURE 11: Parachute test data at an area of 2 m².

FIGURE 12: Parachute test data at an area of 8 m^2 .

The test aims at evaluating the pulling force to a transport aircraft using different dimensions of extraction parachutes. The test diagram is shown in Figure 10. The steps of the test are as follows:

- (1) The parachute rope was fixed on the cargo table at the rail of the transport aircraft by a fastening bolt. The tension sensor and traction parachute latch were fixed on the heavy-weaponry cargo table and the parachute rope passed through the tension sensor.
- (2) The parachute pack for airdrop was hanged at the rear of the cabin. The transport aircraft dragged the parachute and the tension sensor measured the parachute rope tension and saved the data in the storage module.
- (3) After 30–60 s, the parachute opened and was released. The sensor system saved the detail test data in the process of the whole test.

In this test, the sampling frequency of the tension sensor was 200 Hz, the areas of the extraction parachutes were 2 and 8 m^2 , and the length of the parachute lanyard was 35–50 m.

Figure 11 shows the four test results for tension areas of 2 m^2 . They give the tension curves of the ropes from the parachute opening prior to being released. It is obvious that the tension increases rapidly when the parachute opens at the beginning of the curve and decreases rapidly at the end of

TABLE 6: Traction of different parachutes.

No.	2 m^2		8 m^2	
	Maximum (kg)	Average (kg)	Maximum (kg)	Average (kg)
1	788	398	3988	1697
2	883	445	3748	1645
3	872	428	3977	1788
4	853	456	4058	1689
Average	849	432	3943	1705

the curve. During the test, the tension fluctuates violently, which is caused by severe turbulence.

Figure 12 shows the four test results for tension areas of 8 m^2 .

According to the parachute test data, the maximum and average tractions generated by two parachutes, i.e., 2 and 8 m^2 , are shown in Table 6. The traction generated by an 8 m^2 parachute is much bigger than that generated by 2 m^2 parachute, especially the maximum traction. The traction generated by an 8 m^2 parachute is so big that the tension in the rope increases dramatically at the moment of opening the parachute, which is shown in Figure 12.

There is a relation between the weight of the cargo load and the traction needed to pull the cargo out of the cabin,

TABLE 7: Weights of cargo loading.

2 m ²		8 m ²	
Traction (kg)	Weight (kg)	Traction (kg)	Weight (kg)
432	900–2100	1705	3400–8500

which is expressed as traction ratio formula λ of the heavy-equipment airdrop:

$$\lambda = \frac{D_s}{G}, \quad (16)$$

where D_s is the traction resistance and G is the total cargo load. In actual engineering, λ is 0.2–0.5. Using formula (16), we can calculate the weights of the cargo loads that these two parachutes with areas of 2 and 8 m² can pull. The weights of the cargo loads are shown in Table 7.

Table 7 shows that the traction capabilities of 2 and 8 m² extraction parachutes for airdrop are 900–2100 kg and 3400–8500 kg. At the moment of opening, 8 m² parachutes generate the maximum pulling forces of 46 kN.

5. Conclusion

This study designs a triaxial side-pressure tension sensor with a wide range that can be easily installed to measure the parachute tension of airdrop equipment in real time. Temperature error is one of the main errors of the strain sensor, which reaches 1.66% from –20°C to +40°C in the range of 0–100 kN. The LSSVM-PSO algorithm is used to reduce the temperature error of the tension sensor to 0.86%. The sensor was tested and calibrated in Wuxi Institute of Metrology and Testing (WXMTTC). The results show that the repeatability of the sensor is 1.34%, the nonlinearity is 1.03%, and the precision is 3%.

The tension sensor was used in the heavy-equipment airdrop test to measure the average and maximum tension values of extraction parachutes with areas of 2 and 8 m². According to the test, the traction capabilities of two kinds of extraction parachutes for airdrop are 900–2100 kg and 3400–8500 kg. The maximum pulling forces generated by 8 m² parachutes are 10 and 46 kN, respectively. The results of the test can provide a reference to ensure the safe flight of transport aircraft.

Data Availability

The data used to support the findings of this study are currently under embargo while the research findings are commercialized. Requests for data, 6 months after publication of this article, will be considered by the corresponding author.

Conflicts of Interest

The authors declare that they have no conflicts of interest.

Acknowledgments

This research has been funded by the Natural Science Foundation of China (Nos. 51875289 and 61873124), the Aeronautical Science Foundation of China (No. 2016ZD52036), and Jiangsu Province Youth Funding (No. BK20150746).

References

- [1] K. J. Desabrais, J. Riley, J. Sadeck, and C. Lee, “Low-cost high-altitude low-opening cargo airdrop systems,” *Journal of Aircraft*, vol. 49, no. 1, pp. 349–354, 2012.
- [2] J. Chen, C.-B. Ma, and D. Song, “Kinetic characteristics analysis of aircraft during heavy cargo airdrop,” *International Journal of Automation and Computing*, vol. 11, no. 3, pp. 313–319, 2014.
- [3] J. Qiu, X. Y. Wanng, Y. K. Gao, Y. H. Han, and W. J. Hei, “Analysis for heavy cargo airdrop on low altitude based on natural airplane,” *Journal of System Simulation*, vol. 24, no. 4, pp. 933–937, 2012.
- [4] D. C. Meier and S. T. Fiorino, “Application of satellite- and NWP-derived wind profiles to military airdrop operations,” *Journal of Applied Meteorology and Climatology*, vol. 55, no. 10, pp. 2197–2209, 2016.
- [5] D. M. Ștefănescu and M. A. Anghel, “Electrical methods for force measurement—a brief survey,” *Measurement*, vol. 46, no. 2, pp. 949–959, 2013.
- [6] M. Zhao, H. Zhang, R. Zhang, M. Yao, and M. Ma, “Design of surface acoustic wave parafoil riser tension sensor,” *IEEE Sensors Journal*, vol. 17, no. 10, pp. 3022–3029, 2017.
- [7] X. Lu, W. Lu, and C. Zhu, “Compensated SAW yarn tension sensor,” *IEEE Transactions on Instrumentation and Measurement*, vol. 63, no. 12, pp. 3162–3168, 2014.
- [8] V. R. Bagheri, P. H. Tehrani, and D. Younesian, “Optimal strain gauge placement in instrumented wheelset for measuring wheel-rail contact forces,” *International Journal of Precision Engineering and Manufacturing*, vol. 18, no. 11, pp. 1519–1527, 2017.
- [9] Y. Zuo, “Strain gauge measuring system depending on high temperature of aero-engine,” *Computer Measurement & Control*, vol. 16, no. 11, pp. 1528–1529, 2008.
- [10] A. Maskay and M. Pereira da Cunha, “High-temperature static strain langasite SAW sensor: temperature compensation and numerical calibration for direct strain reading,” *Sensors and Actuators A: Physical*, vol. 259, pp. 34–43, 2017.
- [11] W. Lu, Y. Feng, C. Zhu, and J. Zheng, “Temperature compensation of the SAW yarn tension sensor,” *Ultrasonics*, vol. 76, pp. 87–91, 2017.
- [12] T. C. Haber, S. Ferguson, D. Guthrie, T. W. Graver, B. J. Soller, and A. Mendez, “Analysis, compensation and correction of temperature effects on FBG strain sensors,” in *Fiber Optic Sensors and Applications X*, vol. 8722 of *Proceedings of SPIE*, p. 872206, Baltimore, MD, USA, May 2013.
- [13] F. M. Haran, J. K. Rew, and P. D. Foote, “A strain-isolated fibre Bragg grating sensor for temperature compensation of fibre Bragg grating strain sensors,” *Measurement Science and Technology*, vol. 9, no. 8, pp. 1163–1166, 1998.
- [14] X. G. Wang, T. Cai, and F. Deng, “Error compensation of photoelectric encoder based on improved BP neural network,” *Chinese Journal of Scientific Instrument*, vol. 30, no. 7, pp. 1404–1409, 2009.

- [15] J. Nagi, K. S. Yap, and S. K. Tiong, "Detection of abnormalities and electricity theft using genetic support vector machines," in *TENCON 2008 - 2008 IEEE Region 10 Conference*, pp. 1–6, Hyderabad, India, November 2008.
- [16] R. G. Gorjaei, R. Songolzadeh, M. Torkaman, M. Safari, and G. Zargar, "A novel PSO-LSSVM model for predicting liquid rate of two phase flow through wellhead chokes," *Journal of Natural Gas Science and Engineering*, vol. 24, pp. 228–237, 2015.
- [17] B. Sun and H. T. Yao, "The short-term wind speed forecast analysis based on the PSO-LSSVM predict model," *Power System Protection and Control*, vol. 40, no. 5, pp. 85–89, 2012.
- [18] X. Xue, "Prediction of slope stability based on hybrid PSO and LSSVM," *Journal of Computing in Civil Engineering*, vol. 31, no. 1, article 04016041, 2017.
- [19] Y. H. Han and Y. P. Lu, "Dynamics for heavy equipment airdrop and control design," *Flight Dynamics*, vol. 29, no. 3, pp. 28–31, 2011.
- [20] T. Jann, S. Geisbauer, N. Bier, W. Krüger, and H. Schmidt, "Multi-fidelity simulation of cargo airdrop: from the payload bay to the ground," in *AIAA Modeling and Simulation Technologies Conference*, pp. 1–20, Dallas, TX, USA, 2015.

